

In Situ Raman Spectroelectrochemistry of Single-Walled Carbon Nanotubes: Investigation of Materials Enriched with (6,5) Tubes

Ladislav Kavan,^{*,†,⊥} Otakar Frank,^{†,⊥} Alexander A. Green,[‡] Mark C. Hersam,[‡] János Koltai,[§] Viktor Zólyomi,^{§,||} Jenő Kürti,[§] and Lothar Dunsch[⊥]

J. Heyrovský Institute of Physical Chemistry, v.v.i., Academy of Sciences of the Czech Republic, Dolejškova 3, CZ-182 23 Prague 8, Czech Republic, Department of Materials Science and Engineering, Northwestern University, Evanston, Illinois 60208-3108, Department of Biological Physics, Eötvös Loránd University, Pázmány Péter sétány 1/A H-1117 Budapest, Hungary, Research Institute for Solid State Physics and Optics of the Hungarian Academy of Sciences, P.O. Box 49, 1525 Budapest, Hungary, and Leibniz Institute of Solid State and Materials Research, Helmholtzstrasse 20, D-01069 Dresden, Germany

Received: January 17, 2008; Revised Manuscript Received: May 21, 2008

Single-walled carbon nanotubes (CoMoCat) have been enriched with (6,5) tubes via density-gradient ultracentrifugation. Thin solid films of quasi-isolated nanotubes were fabricated from a solution of sorted nanotubes by vacuum filtration and extraction with water. Optical spectroscopy in the vis–NIR region and Raman spectroscopy were used to characterize these materials. The experimental studies were supported by a theoretical analysis of the electronic and vibrational structure of selected (*n,m*) tubes by using density functional theory. Besides the most abundant tubes (6,5), the experimental and theoretical data for tubes (6,4), (7,3), (7,5), (8,3), and (9,1) are also discussed. A detailed investigation by in situ Raman spectroelectrochemistry was focused on the effects of electrochemical p/n-doping. The experimental analysis of the intensities and frequencies of the radial breathing mode and the tangential displacement modes were correlated with the theoretically calculated optical transition energies and Raman frequencies. It was demonstrated that electrochemical charging is a useful tool for the study of doping effects on the electronic structure of carbon nanotubes.

1. Introduction

Since the pioneering studies in 1999–2000,^{1–3} in situ Raman spectroelectrochemistry has developed into an important technique of characterization of single-walled carbon nanotubes (SWNTs).⁴ Besides small and complicated shifts of Raman frequencies,^{4,5} the electrochemical charge-transfer in SWNT significantly influences the intensity of Raman scattering. This effect is caused by the suppression of resonance enhancement due to quenching of allowed optical absorptions in SWNT.⁴ In general, the intensity of Stokes Raman scattering, I_{Raman} , scales with the optical transition energy of the molecule, ΔE_{ii}

$$I_{\text{Raman}} \cong |(E_L - \Delta E_{ii} - i\gamma)[E_L - \Delta E_{ii} - E_{\text{ph}} - i\gamma]|^{-2} \quad (1)$$

where E_L is the laser photon energy, E_{ph} is the phonon energy, and γ is the damping constant, describing the relaxation of the excited state. In SWNTs, the optical transition energies, ΔE_{ii} , were mostly identified with the separation of Van Hove singularities (VHS) in the density of electronic states (DOS). This approach obviously neglects the electron–hole interaction in the photoexcited state, *viz.* the excitonic effects.^{4,6} Nevertheless, following the philosophy of the experimental Kataura plot^{7–9} these theoretical problems (cf. refs 4, 10) can be bypassed by using the experimental values of ΔE_{ii} available from optical spectroscopy, photoluminescence, or resonance Raman spec-

troscopy. For instance, the Raman spectra of (6,5) and (6,4) tubes, measured with the yellow line of Kr^+ laser (2.18 eV), are resonance enhanced through optical transitions at ca. 2.15 and 2.10 eV, respectively,^{11–13} and within the traditional approach, we can identify these transitions with ΔE_{22} in semiconducting tubes.

Except for several studies of single SWNT,^{14,15} the Raman spectroelectrochemistry has thus far been applied to conventional SWNTs samples containing a mixture of bundled tubes of varying chiral indices. The reason is that an investigation of single SWNT is experimentally demanding with sample instability (electrochemical “corrosion”)¹⁵ being among the crucial technical difficulties to be addressed. However, experiments on an ensemble of SWNTs are not easy, either, because of overlapping signals from various tubes and the effect of bundling of SWNTs, which is omnipresent in the as-grown samples. The bundling causes a red shift of optical transition energies and decreases the accessible surface area both for adsorption of gaseous molecules (BET isotherms) and electrolyte ions.⁴ During electrochemical treatment, the electrolyte counterions decorate mostly the outer surface of a bundle at the usual electrode potentials. Hence the spectroelectrochemistry of a bundle is convoluted not only by the presence of many tubes but also by their different feedback to charging, which depends on the localization of the given tube either in the interior or on the surface of a bundle.⁴

The investigation of SWNT mixtures at the level of chirality-specific Raman spectroelectrochemistry has thus far been limited solely to HiPco nanotubes, because they show quite resolved radial breathing mode (RBM) bands, and some of them are assignable to the (*n,m*)-identified nanotubes.^{16,17} The discovery

[†] Academy of Sciences of the Czech Republic.

[⊥] Leibniz Institute of Solid State and Materials Research.

[‡] Northwestern University.

[§] Eötvös Loránd University.

^{||} Research Institute for Solid State Physics and Optics of the Hungarian Academy of Sciences.

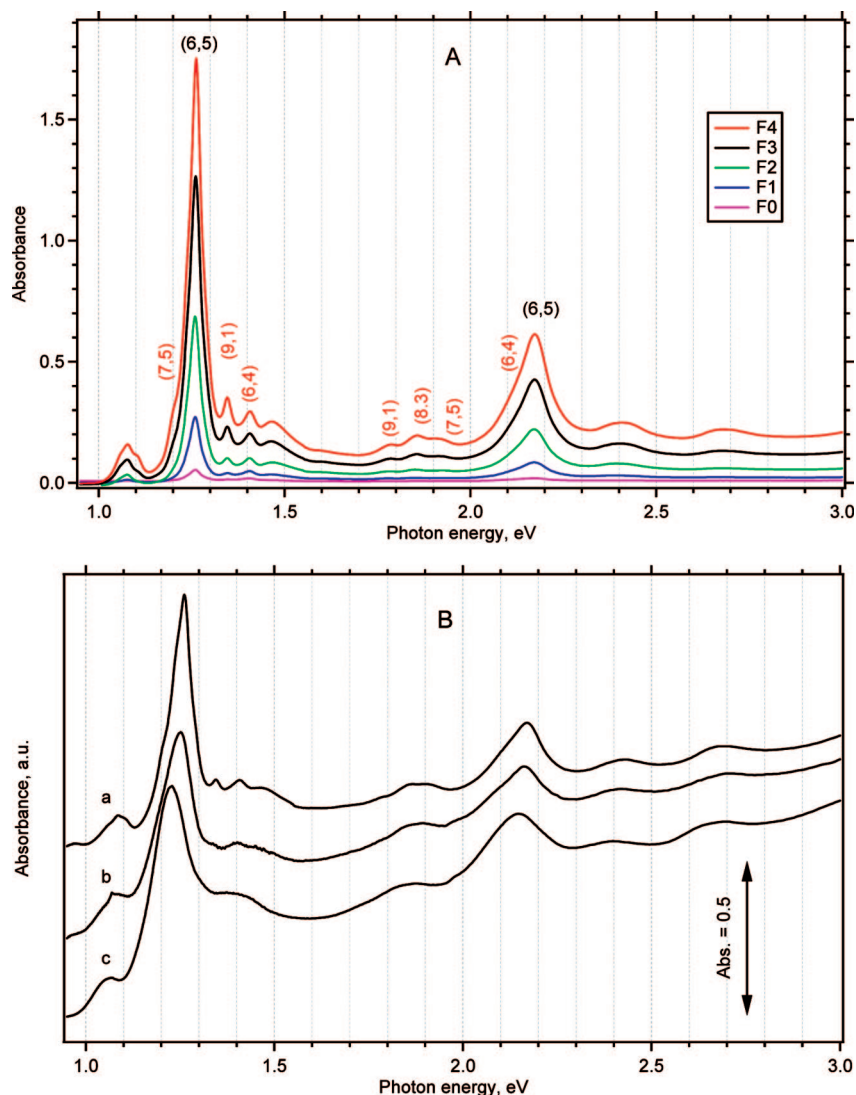


Figure 1. Optical spectra of the studied SWNT samples. (A) Spectra of sorted SWNTs (samples F0–F4) in solutions; the optical cell thickness was 1 cm. (B) Comparison of the spectra of solution and solid films on glass made from the “raw” sample. (a) Solution; optical cell thickness 1 mm, (b) dry film cast from a solution of SWNT-raw on glass and evaporated, (c) dry film from water-extracted SWNT-raw evaporated on glass. The spectra in chart B are offset for clarity, but the absorbance scale is identical for all plots. The scale bar represents the absorbance of 0.5.

of ultracentrifugal sorting of SWNT¹⁸ has brought a new impulse into this story, because it provides the (n,m) -enriched and nonbundled SWNT in reasonable quantities. This paper presents the first study of ultracentrifugally sorted SWNT samples, which are enriched with (6,5) tubes.

2. Experimental Section

The sample of sorted nanotubes was prepared by dispersing CoMoCat nanotubes in sodium cholate aqueous solution using vigorous horn ultrasonication. (CoMoCat is an acronym for SWNT made by decomposition of carbon monoxide using a Co/Mo catalyst). The raw material was purified by ultracentrifugation at 288 000*g* for 32 min to remove large aggregates. Sorted samples were prepared by density gradient ultracentrifugation in aqueous solution of iodixanol as described in refs 18, 19. Samples F0 to F4 were obtained from neighboring layers in the same density gradient, with F0 being the least dense material and F4 being the most. However, since the sorted samples were obtained from only a small region in the gradient, the differences in their composition are not expected to be significant.

Sorted SWNT solutions enriched in the (6,5) chirality were recovered from the density gradient, vacuum filtered through a 0.22 μm membrane filter (mixed cellulose esters, Millipore), and washed with excess of water to remove sodium cholate and iodixanol. After drying at 70 $^{\circ}\text{C}$ in vacuum overnight, the filter was placed onto a glass slide, and the cellulose membrane was dissolved with acetone. Optical absorption spectra of the solutions and the thin solid films on glass were measured by a double-beam Shimadzu 3100 spectrometer in the 280–2600 nm range and by a Lambda 19 (Perkin-Elmer) spectrometer in the 300–3200 nm range, both with 1 nm spectral resolution.

For Raman spectroscopy, the solutions of SWNT were vacuum-filtered through a PTFE membrane (0.2 μm pore size, Whatman) and washed with water. The filter with a SWNT-film on top was dried in air, cut into small pieces, and transferred into ethanol. After short sonication (ca. 5 min), most of the tubes delaminated from the filter into the ethanolic medium. A droplet of this suspension was evaporated on top of a Pt disk electrode sealed in glass. The electrode was outgassed overnight at 70 $^{\circ}\text{C}$ in vacuum (10^{-1} Pa) and then mounted into a Raman spectro-electrochemical cell in a glovebox under nitrogen. The cell was

equipped with Pt-counter and Ag-wire pseudoreference electrodes, and 0.2 M LiClO₄ in dry acetonitrile (Aldrich) was the electrolyte solution. The potential of the pseudoreference electrode was calibrated after adding a small amount of ferrocene to the electrolyte solution at the end of each series of spectroelectrochemical tests. Hence, all potentials were referred to the ferrocene reference electrode, Fc/Fc⁺.

Electrochemical doping was carried out potentiostatically (PG 300-potentiostat, HEKA, Germany). Bold lines in the Raman spectra (cf. Figures 3 and 4 below) denote measurements at the applied potential of 0 V vs Ag-pseudoreference (ca. −0.35 V vs Fc/Fc⁺). Open-circuit potentials of the SWNT-covered Pt electrode in a freshly assembled cell were between −0.3 to −0.5 V vs Fc/Fc⁺. Spectra were excited by Kr⁺ and Ar⁺ lasers (Innova 300 series, Coherent) and recorded by a T-64000 spectrometer (Instruments, SA) interfaced to an Olympus BH2 microscope. The laser power impinging on the cell window was between 2 and 5 mW. The Raman spectrometer was calibrated before each set of measurements by using for reference the F_{1g} line of Si at 520.2 cm^{−1}. All frequencies and intensities at the given excitation wavelength were normalized against the Si-line. A second convenient reference, both for intensities and frequencies, are the bands of acetonitrile at 378.5 and 1375.5 cm^{−1}, which serve as an internal standard in spectroelectrochemistry of nanotubes.^{20,21}

3. Theoretical Section

Calculations were carried out for the frequencies of the totally symmetric modes, the RBM and the G[−] part of the tangential modes, as well as for the electronic DOS of several small diameter tubes: (5,3), (6,1), (6,4), (6,5), (7,3), (7,5), (8,3), and (9,1). The calculations were done with density functional theory (DFT) using the Vienna *ab initio* simulation package (VASP) code²² at the local density approximation (LDA) level and projector augmented-wave (PAW) method. After optimization of the geometry, the frozen phonon approximation was used to obtain the frequencies in the coupled three-dimensional space of the totally symmetric vibrations.^{23,24} For the determination of the DOS, 30 or 10 irreducible k-points were used (1 × 1 × 60 or 1 × 1 × 20 Monkhorst-Pack grid, centered around Gamma point), depending on the number of atoms in the primitive cell.

4. Results and Discussion

Figure 1 shows the optical spectra of sorted and raw nanotubes. The spectra are dominated by peaks corresponding to ΔE_{11}^S and ΔE_{22}^S transitions of the (6,5) tube. Also some other individual tubes can be recognized in the spectra as indicated in Figure 1A. Comparing the spectra of raw and sorted samples (Figure 1B-a vs Figure 1A), the peaks belonging to the (6,5) tube become narrower in the sorted samples, clearly demonstrating the enrichment of the (6,5) tubes content in this sample. Table 1 summarizes the estimated composition of the semiconducting chiralities in the sorted materials. The concentrations of the particular tubes were determined by fitting the optical absorbance data to Lorentzians defined using transition energies reported in ref 25. Since, however, the contributions from chiralities such as (6,5) and (8,3) have overlapping transitions, the uncertainty in the compositions reported here is ~5%. The density gradient ultracentrifugation can increase the relative concentration of minority chiralities. Hence, it is not surprising that the (7,5) and (8,3) tubes, which are difficult to detect in the starting material, are enriched in the sorted material (Table 1).

TABLE 1: Estimated Proportions of Semiconducting Nanotubes in the Raw and Sorted SWNT Material As Determined from Optical Spectra^a

chirality		estimated composition of semiconducting species, %					
<i>n</i>	<i>m</i>	raw material	F0	F1	F2	F3	F4
6	4	15	9	7	7	6	7
6	5	56	78	79	74	70	43
7	3	9	7	9	9	7	19
7	5	0	0	0	0	2	12
8	3	0	0	0	1	4	7
8	4	1	0	0	0	0	3
8	6	1	0	0	0	0	0
8	7	1	0	0	0	0	0
9	1	7	4	5	6	6	6
9	2	2	0	0	3	4	3
9	5	3	0	0	0	0	0
9	7	3	0	0	0	0	0
10	0	2	0	0	0	0	0

^a The composition is expressed in % of nanotubes. (It can also be assumed in wt% if there is no dependence on length for the different chiralities).

TABLE 2: DFT Calculated Values of the Optical Transitions ΔE_{11} and ΔE_{22} for Several SWNTs (all values are in eV)

(n,m)	<i>N_C</i> ^a	ΔE_{11}						ΔE_{22}	
		ΔE_{11}^b	$1.3 \times \Delta E_{11}$	(exp)	ΔE_{22}^c	$1.2 \times \Delta E_{22}$	(exp)		
(5,3)	196	1.21	1.57	-	1.93	2.32	-		
(6,4)	152	1.12	1.46	1.41	1.78	2.14	-		
(6,5)	364	0.96	1.25	1.26	1.83	2.20	2.17		
(7,3)	316	0.93	1.21	-	1.76	2.11	-		
(7,5)	436	0.94	1.22	-	1.58	1.90	1.91		
(8,3)	388	1.04	1.35	-	1.53	1.84	1.86		
(9,1)	364	1.05	1.37	1.35	1.47	1.76	1.79		

^a *N_C* is the number of carbon atoms in the unit cell. ^b The 30% upscaled ΔE_{11} numbers are comparable with the experimental values obtained from the optical spectra in solution (cf. Fig. 1). ^c The 20% upscaled ΔE_{22} numbers are comparable with the experimental values obtained (where available) from ref 12.

Chart B of Figure 1 depicts the differences between a solution and solid films made of SWNT (raw). In the surfactant-stabilized solution, the ΔE_{11}^S transition of the (6,5) tube corresponds to an optical absorption peak at 1.260 eV (curve a). Curve b in Figure 1B shows a spectrum of a solid film made by evaporation of this solution. Although this film still contains the original amount of surfactants, we can trace the ΔE_{11}^S maximum shifted toward 1.251 eV. The purified film from a water-extracted material (curve c) exhibits the ΔE_{11}^S maximum at 1.228 eV. Obviously, the solid films have red-shifted optical maxima due to stronger tube–tube interaction in the films, and the minor peaks for the other chirality components tend to merge. The solution/film red-shift amounts 32 meV for the ΔE_{11}^S transition but only 22 meV for the ΔE_{22}^S transition of the (6,5) tube. The latter transition is crucial for resonance enhancement of our Raman spectra, *vide infra*.

Table 2 summarizes the DFT calculated transition energies of ΔE_{11} and ΔE_{22} for several tubes with small diameters. Also shown are the experimental values from optical spectra in solutions (cf. Figure 1).

It is well-known that DFT underestimates the excitation energies. However, by an appropriate upscaling (30% for ΔE_{11} and 20% for ΔE_{22}) the corresponding theoretical and experimental values are in good agreement. The empirical scaling factors are justified from the comparison of our calculated and measured values and also from the earlier literature²⁶ reporting

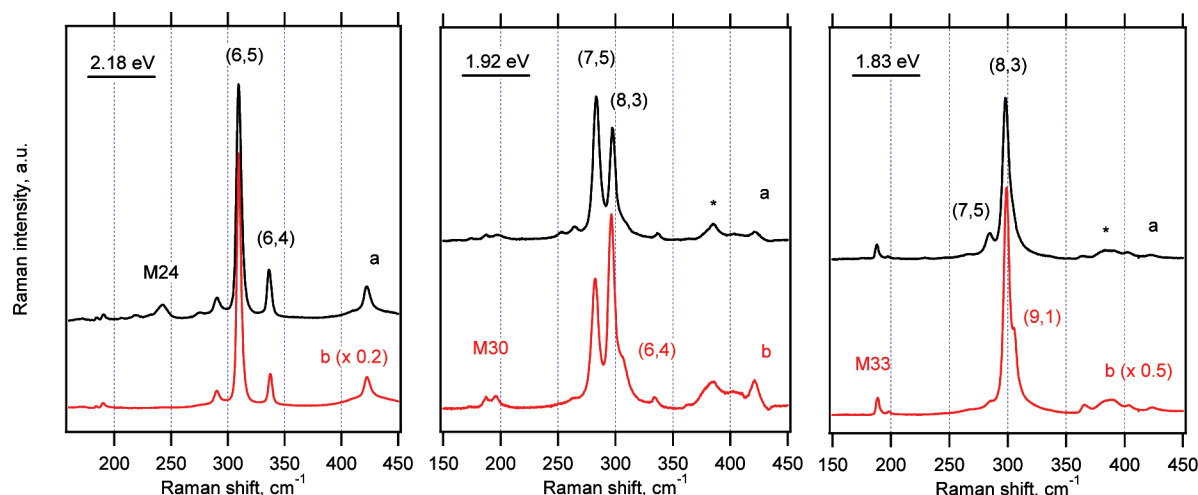


Figure 2. Raman spectra of dry nanotube film on top of the PTFE filter (see Experimental Section for details). Curves a are for a raw material; curves b are for a sorted material (sample F1). Note that the intensities for curves b are scaled in the left and right plots as indicated. The features at 380 cm^{-1} (marked by *) come from the PTFE filter.

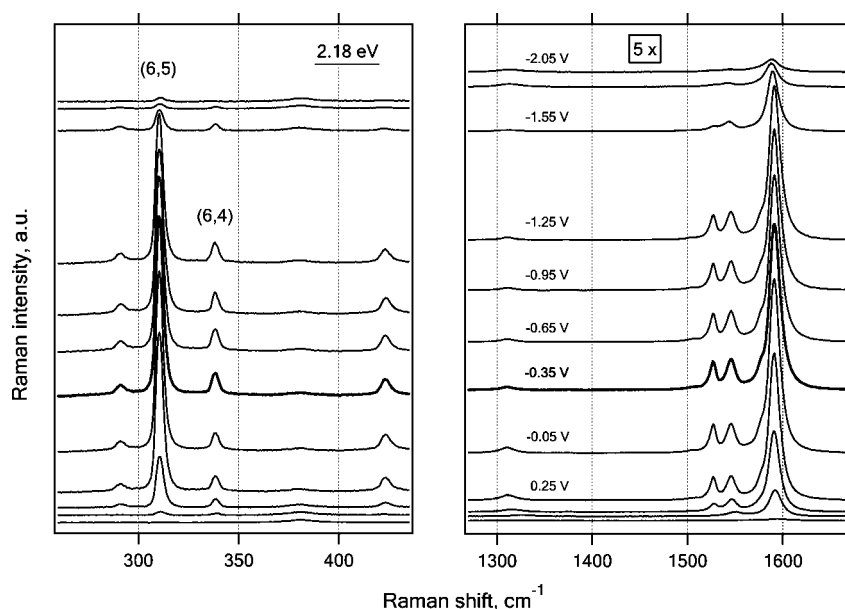


Figure 3. Raman spectra of SWNT (excited by Kr^+ laser at 2.18 eV) in $0.2\text{ M LiClO}_4 + \text{acetonitrile}$ solution. The electrode potential (in V vs Fc/Fc^+) was for curves from top to bottom: -2.05 , -1.85 , -1.55 , -1.25 , -0.95 , -0.65 , -0.35 (bold line), -0.05 , 0.25 , 0.55 , 0.85 , 1.05 . Spectra are offset for clarity, but the intensity scale is identical in the respective window. Left chart shows the same spectra with intensity scale smaller by a factor of 5. Bold line denotes a spectrum of nearly undoped sample; see Experimental Section for details.

that the LDA calculated excitation energies need to be upscaled by about 1.2.

Figure 2 presents the Raman spectra in the RBM region of dry nanotube film as made on the PTFE filter (see Experimental Section). For comparison, the spectra of raw material (curves a) and the sorted material (sample F1; curves b) are plotted in Figure 2. The spectra are expectedly dominated by the signal of the tubes (6,5) because the sample is enriched by these tubes. From optical absorbance, we estimate that $\sim 79\%$ of the semiconducting species in F1 are of (6,5) chirality compared to $\sim 56\%$ content of (6,5) in the raw CoMoCat material (cf. Table 1). Also the tubes (6,4), (7,5), and (8,3) are unambiguously detected with the yellow and red lasers. Interestingly, the tube (6,4) is traceable even at the 1.92 eV excitation, despite being ca. 0.2 eV off-resonance for this laser. (Strictly speaking, we may speculate that this peak is not the RBM of the tube (6,4) but a Raman peak of iodixanol from the sorting process.¹⁸ However, the assignment to iodixanol impurity is not supported by spectroelectrochemistry; see below.) The tube (6,5) would

be ca. 0.25 eV off-resonance at the same conditions, but it is not that clearly distinguished in Figure 2 (midplot) because of an overlap with (8,3) and (9,1) tubes.

The spectra in Figure 2 curve b are for the sample F1 having the highest concentration of (6,5) tube (cf. Table 1). Nevertheless, the spectra of sorted samples (F0–F4) did not depend significantly on the level of sorting enrichment (data not shown). This is obviously due to the highly selective resonance enhancement in the Raman spectra of certain tubes, which overrides the effect of sample enrichment. However, the sorting caused disappearance of metallic tubes of the M24 family, which resonate with the yellow laser, but some other metallic tubes (M30 and M33 resonating with the red lasers) are still present in the sorted sample (Figure 2).

Table 3 compares the measured RBM Raman frequencies positions with the DFT calculated ones. The agreement is very good. The $2\text{--}3\text{ cm}^{-1}$ systematic underestimation in the calculation is probably attributed to surfactant and/or bundling effects, which cause the measured frequencies to be higher than the

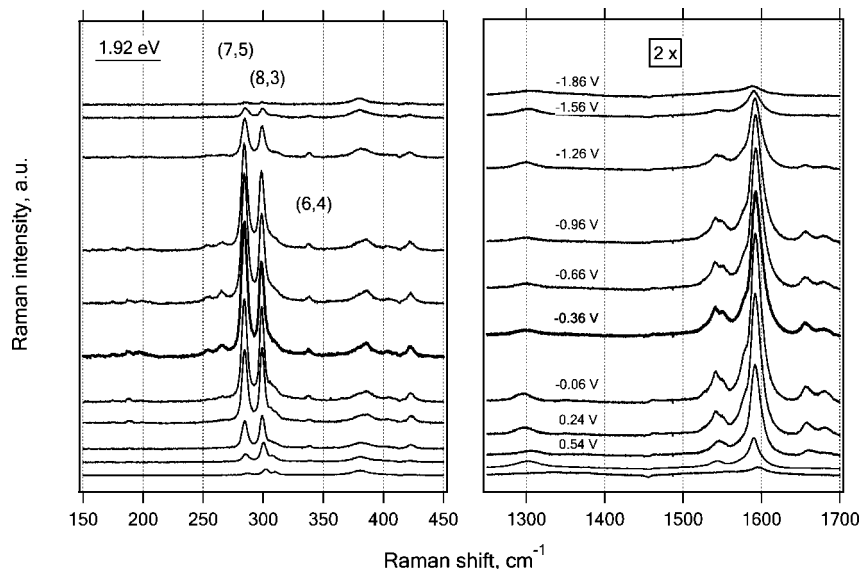


Figure 4. Raman spectra of SWNT (excited by Kr⁺ laser at 1.92 eV) in 0.2 M LiClO₄ + acetonitrile solution. The electrode potential (in V vs Fc/Fc⁺) was for curves from top to bottom: −1.86, −1.56, −1.26, −0.96, −0.66, −0.36 (bold line), −0.06, 0.24, 0.54, 0.84, 1.14. Spectra are offset for clarity, but the intensity scale is identical. Bold line denotes a spectrum of nearly undoped sample; see Experimental Section for details.

TABLE 3: Calculated Diameters (in nm) and Vibrational Frequencies (in cm^{−1}) for Several SWNTs

(<i>n,m</i>)	<i>d</i> _{DFT} ^a	<i>d</i> ₀ ^b	<i>d</i> ₀ ^{*b}	ω_{RBM} (calc)	ω_{RBM} (exp) ^c	ω_{G} (calc)	ω_{G} (exp) ^c
(5,3)	0.554	0.556	0.545	414	422	1516	-
(6,1)	0.522	0.521	0.511	433	422	1523	-
(6,4)	0.686	0.692	0.679	333	336	1523	1527
(6,5)	0.749	0.757	0.743	307	309	1544	1545
(7,3)	0.699	0.706	0.693	329	-	1540	-
(7,5)	0.819	0.829	0.813	281	283	1556	-
(8,3)	0.774	0.782	0.767	296	298	1551	-
(9,1)	0.750	0.757	0.743	304	-	1547	-

^a The diameters *d*_{DFT} were taken from the DFT optimized geometry. ^b The diameters *d*₀ and *d*₀^{*} were calculated by using the usual “wrapping” formula (eq 2) assuming a C–C bond length of 0.144 nm (ref 25) and 0.1413 nm (ref 23), respectively. ^c For comparison, the experimental values of Raman frequencies are also shown.

calculated ones. Of particular interest is the peak at 422 cm^{−1}, which is detectable with yellow and red lasers, and is well pronounced at the 2.18 eV excitation (cf. Figure 2). The DFT calculated RBM frequency for the (5,3) tube is 414 cm^{−1}, and ΔE_{22} is 2.3 eV (after 20% upscaling); see Tables 2 and 3. The calculated ΔE_{22} is in good agreement with the experimental value reported by Weisman and Bachilo ($\Delta E_{22} = 2.374$ eV from photoluminescence).²⁵ We may note that the same authors also calculated a similar RBM frequency [as $(223.5/d_0) + 12.5 = 414.7$ cm^{−1}] (ref 25). The other candidate, besides (5,3), for the assignment of our peak at 422 cm^{−1} seems to be the tube (6,1) for which our DFT calculated RBM frequency is 433 cm^{−1}, and ΔE_{22} is 2.0 eV (after 20% upscaling).

Table 3 summarizes the diameters of our studied tubes, too. The values *d*₀ were calculated using the popular “wrapping formula”

$$d_0 = \frac{a_{\text{C-C}}\sqrt{3}}{\pi}\sqrt{n^2 + m^2 + nm} \quad (2)$$

where *a*_{C–C} is the distance of C-atoms, *a*_{C–C} = 0.144 nm (ref. 25). The values *d*_{DFT} (Table 3) are taken from the DFT optimized geometry. The fact that *d*_{DFT} < *d*₀ virtually contradicts our earlier

conclusion that, for increasing curvature, the tube should be blown up, because of the increasing repulsive interactions between the components of the tube.²³ This paradox is rationalized, if we use the “ideal wrapping” data, which means the same formula (eq 2) but with the *a*_{C–C} distance of 0.1413 nm. This is the optimized value for graphene, using exactly the same DFT method as what was used for the tubes.²³

Figures 3 and 4 show the Raman spectroelectrochemical plots for sorted SWNTs at the 2.18 and 1.92 eV excitations, respectively. They confirm the doping-induced attenuation of the Raman intensities, which is roughly symmetrical toward cathodic and anodic charging (Figure 5). This conclusion is not trivial with respect to our previous study of HiPco tubes.¹⁷ According to an empirical “resonance rule”,^{16,17} the Raman intensities of tubes, which are in good resonance with the exciting or scattered photons, are the most sensitive toward doping-induced attenuation and *vice versa*. Consequently, the tubes whose ΔE_{ii} are slightly larger (by ≈ 0.1 eV) than the energy of the exciting photon exhibit this effect most clearly (cf. eq 1); in other words, they are less sensitive to charge-transfer doping.^{4,16,17}

There was only one explicit exception to this resonance rule: The tube (6,5) in the previously studied HiPco samples was doping-silent at 2.18 eV laser line, even though it is in almost optimum resonance at these conditions.¹⁷ We have speculated that this HiPco-borne (6,5) tube was, actually, not a true SWNT, but an *inner* tube in a double-walled nanotube (DWNT),¹⁷ which would explain its anomalous insensitivity to doping.^{27,28} Our data in Figure 3 elucidate further this earlier paradox: The tube (6,5) in our sorted CoMoCat material behaves “normally” in terms of the resonance rule. Hence, this supports our previous conclusion that the behavior of the tube (6,5) in the HiPco sample was, indeed, exceptional.¹⁷

Recently, Takeda and Murakoshi²⁹ noted that the resonance rule is also perturbed by bundling of SWNTs, which causes a red shift of optical transitions and broadening of Raman excitation profiles. The reported red shifts between an aqueous solution of surfactant-wrapped SWNTs and the same SWNTs bundled were between 0.054 to 0.157 eV.^{8,30} However, in our case, the optical absorption maxima in solution and glass-supported solid film were not that different (cf. Figure 1). For

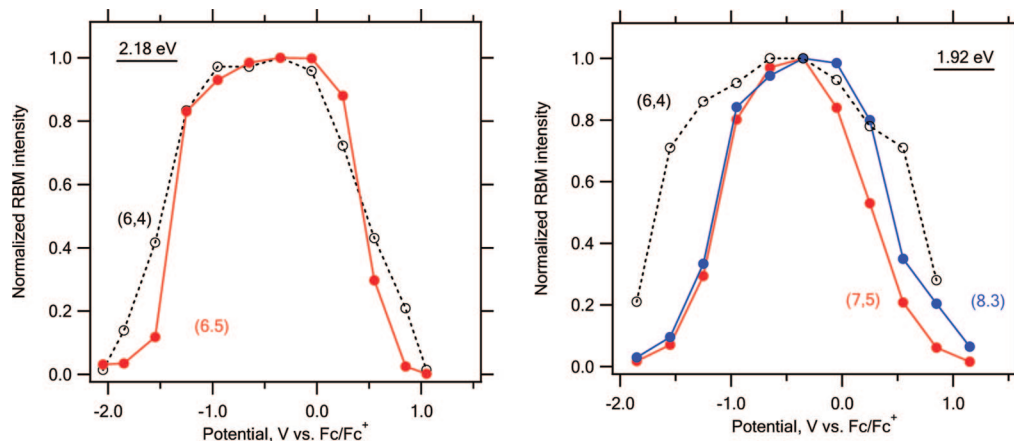


Figure 5. Intensity of the RBM-line as a function of the applied electrode potential in 0.2 M LiClO₄ + acetonitrile solution at two different excitation laser energies (2.18 and 1.92 eV). The intensities were normalized by assigning 1 to the maximum RBM intensity. Assignment of the curves to the particular (*n,m*) tubes is labeled.

instance, the experimentally found ΔE_{22} of (6,5) in the purified (water-extracted) film was 2.15 eV. The same transitions of sodium cholate-encapsulated (6,5) in solution was only ca. 0.02 eV blue-shifted. Hence, the SWNTs in our films are probably quasi-isolated by the surfactant.

We should note that the distinct peak at 336 cm⁻¹ assigned to the (6,4) tube in Figure 2 (middle chart; 1.92 eV excitation) is, indeed, a tube-related feature. It does not appear to belong to the iodixanol impurity discussed above. The assignment to the tube's RBM consists of its marked spectroelectrochemical tuning of intensities seen in Figure 4. (Obviously, the charging-induced intensity attenuation would be absent for iodixanol).

The Raman peak at 422 cm⁻¹ (cf. Figure 2) shows the "normal" charging-induced attenuation at 2.18 eV (Figure 3) but is markedly less sensitive to doping at 1.92 eV (Figure 4). This would indicate its assignment to nanotube features having an optical transition near 2.18 eV. If we assume that this peak is due to the RBM, there are only two assignable tubes, viz. (5,3) and (6,1). The closest tube seems to be the (5,3) having RBM = 414.7 cm⁻¹ and ΔE_{22} = 2.374 eV.²⁵ (see also Tables 2 and 3 and discussion above). The assignment to (5,3) is further supported by the fact that the peak at 422 cm⁻¹ is detectable also with the green Ar⁺ laser (2.41 eV), and it exhibits a pronounced charging-induced attenuation at the 2.41 eV excitation, (data not shown).

In Figure 5, the difference of the potential dependence between the tubes with distinct chiralities is small. This contradicts some earlier work on the electrochemical¹⁴ and chemical³¹ doping of SWNT, which reports on the significant and monotonic increase of the work function (WF) with the band gap (inverse diameter) of SWNT. If we assume that the maximum of the intensity/potential profile is equal to the Fermi level position (E_F = -WF),¹⁴ all of our tubes exhibit this maximum near -0.5 V vs Fc/Fc⁺ (which is supposed to be their Fermi level in the electrochemical scale). However, according to the cited work,^{14,31} this potential should be ca. 0.3 V more positive for the (6,4) tube compared to that of the (7,5) tube. Our data in Figure 5 obviously do not support this prediction. The relative insensitivity of E_F on the tube diameter is further corroborated by an analogous study of HiPco tubes which all exhibited the intensity/potential profile peak near -0.5 V vs Fc/Fc⁺.¹⁶ Recently, Paolucci et al.³² have found a similar diameter insensitivity of E_F based on optical spectroelectrochemistry of SWNTs in solution. Hence, the effect of the diameter (band gap) on the absolute position of the Fermi level

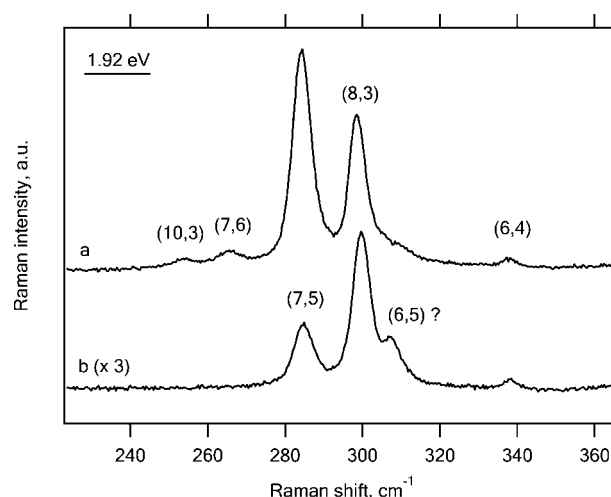


Figure 6. Detail of the Raman spectroelectrochemical plot of SWNT (excited by Kr⁺ laser at 2.18 eV) in 0.2 M LiClO₄ + acetonitrile solution. Curve a measured in nearly undoped state (at -0.36 V vs Fc/Fc⁺). Curve b measured at 0.84 V vs Fc/Fc⁺. The Raman intensity is zoomed by a factor of 3.

seems to be small, if any. Also recent theoretical calculations^{33–35} show that the relative changes can even be nonmonotonic for varying diameters, and, in general, they are much smaller than assumed in the earlier reports.^{14,31}

We have investigated this question theoretically, by carrying out DFT calculations, using the VASP code, to obtain the Fermi level for all four tubes given in Figure 5. In order to get the correct absolute values, the vacuum potentials were also calculated. The results for the (vacuum potential corrected) Fermi levels were -4.592 eV (6,4), -4.557 eV (6,5), -4.559 eV (8,3), and -4.523 eV (7,5). This demonstrates that (i) the change in the Fermi energies is less than 0.1 eV, and (ii) the diameter dependence is nonmonotonic.

Figure 6 shows a zoomed detail of the Raman spectroelectrochemical plot at 1.92 eV excitation. Curve a is for a SWNT in a nearly undoped state, and curve b is for the same sample after strong p-doping at the electrode potential of 0.84 V vs Fc/Fc⁺. The pristine sample (Figure 6, curve a) contains the expected tubes (7,5), (8,3), and (6,4). Furthermore, there are two distinct peaks assigned to (7,6) and (10,3) tubes, which were not traced by optical spectroscopic analysis (Table 1 and Figure 1). Since these two tubes are in good resonance with the 1.92 eV laser, their detection by Raman spectroscopy is

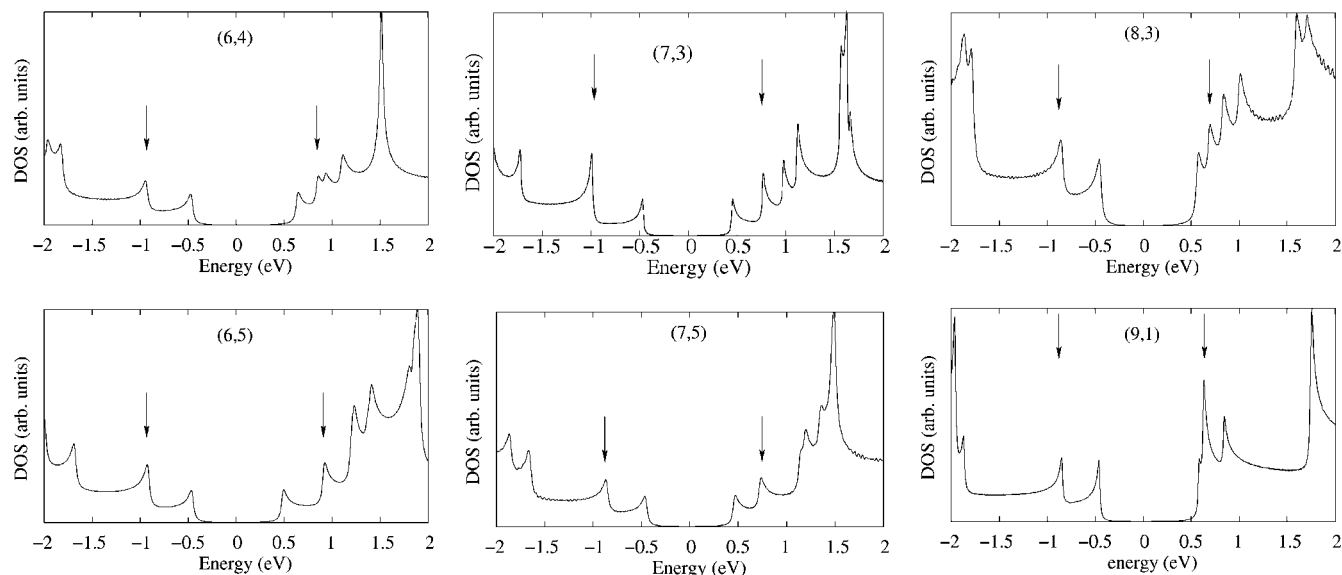


Figure 7. Density of states calculated by the DFT method for selected tubes. The arrows indicate the VHSs involved in the ΔE_{22} transition. The Fermi energies are set to zero in all cases.

sensitive enough, and, second, their complete quenching in the p-doped sample (curve b) reconfirms the assignment, because this is a specific signature of well-resonating tubes.^{16,17} The same argument (resonance rule)^{16,17} is also applicable for interpreting the different intensity attenuation of (7,5) and (8,3) tubes upon p-doping (Figure 6, curves a, b). From Table 2, the ΔE_{22} values for (7,5) and (8,3) tubes are 1.91 and 1.86 eV, respectively. Hence, the tube (7,5) is more doping-sensitive, because it is in better resonance with the 1.92 eV laser. On the other hand, the off-resonance tube (6,4) ($\Delta E_{22} \sim 2.14$ eV, Table 2) is still resolved in curve b of Figure 6, because it is almost doping-silent at these conditions.^{16,17} The most explicit effect of p-doping is the emergence of a new peak at 307 cm^{-1} which is not found in the undoped tubes (Figure 6). It is tempting to assign it to the off-resonance tube (6,5) ($\Delta E_{22} \sim 2.17$ eV, Table 2), because it is the dominating tube in our enriched sample. However, there is a possible overlap with the (9,1) tube, which is also slightly off-resonance but in the opposite direction ($\Delta E_{22} \sim 1.79$ eV, Table 2). Although the spectral assignment of the peak at 307 cm^{-1} is not unique in this particular case, the usefulness of the resonance rule for spectroelectrochemical “deconvolution” of Raman spectra is obvious.

The G-band (Figures 3 and 4) exhibits the expected blue/red shift upon anodic/cathodic charging.⁴ Of particular interest is the splitting of the G^- band, which is well pronounced for the yellow laser (Figure 3). The frequency of G^- band, ω_G , is known to scale with the tube diameter, d

$$\omega_{G^-} = \omega_0 + \frac{\beta}{d^n} \quad (3)$$

with $\omega_0 \approx 1591 \text{ cm}^{-1}$ (frequency of the G^+ -band), $n \approx 2$, and $\beta = -45.7 \text{ cm}^{-1} \cdot \text{nm}^{-2}$ or $-79.5 \text{ cm}^{-1} \cdot \text{nm}^{-2}$ for semiconducting tubes or metallic tubes, respectively.³⁶ The found ($\omega_G - \omega_0$) values are 64 and 46 cm^{-1} (Figure 3). The calculated (eq 3) ones are 99 and 81 cm^{-1} for the tubes (6,4) and (6,5), respectively. The difference might be due to that fact that the cited correlation (eq 3) was, actually, determined for considerably wider tubes (d ranging between 0.95 and 2.62 nm).³⁶

To gain deeper insight into this discrepancy, we have modeled the G^- frequencies by DFT calculations. The calculated G^- frequencies are 1523 cm^{-1} and 1544 cm^{-1} for (6,4) and (6,5),

respectively (Table 3). The agreement with the measured values of 1527 cm^{-1} and 1545 cm^{-1} is very good. Hence, we assume that for thinner tubes ($d < 1$ nm), the coefficients in the correlation (represented by eq 3) deviate from the reported values which were derived for $d > 1$ nm.³⁶ If we assign the low-frequency G^- (1527 cm^{-1}) to the tube (6,4) and the high-frequency G^- (1545 cm^{-1}) to the tube (6,5), it is interesting to note that the former attenuates more significantly with charging (Figure 3). Obviously, this potential-dependent behavior is opposite to that of the RBM (Figures 3–5). Recently, Das et al.⁵ presented a similar theoretical and experimental study of Raman spectroelectrochemical behavior of G^+/G^- bands in metallic and semiconducting tubes.

The intensity/electrode-potential profiles in Figure 5 seem to reflect not only the “resonance rule” but also the individual electronic structure of the particular tube. Figure 7 shows the electronic DOS for the tubes (6,5), (6,4), (9,1), (7,3), (7,5), and (8,3) as they were obtained from DFT calculations, without any scaling. As it was mentioned above, upscaling by about 30% leads to an improved agreement with the experimental data. The calculation of the exact Raman intensity/potential profiles (experimental values seen in Figure 5) is difficult on the DFT level. Not only the excitation energies but also the transition matrix elements are needed to calculate the Raman intensity. However, a semiquantitative explanation of the differences in the quenching of RBM intensities for different tubes can be given.

The explanation was based on the validity of the ‘rigid band’ approximation. First, it was checked that this approximation is applicable for doping studies. Figure 8 shows that the DOS of (6,5) has only shifted with a very small change of the shape, even for rather high doping levels of 0.01 e/C and 0.05 e/C. The ‘rigid band’ approximation is quite good even up to 0.05 e/C charging. The vertical lines in the plot show the position of the Fermi level, which correspond (except for the neutral case) to the position of the highest occupied states for n-doping to different levels. It is clearly seen that for 0.01 e/C the Fermi level is still below the “ E_{22} -band” in the DOS, whereas for 0.05 e/C the Fermi level is already above this band. Within the ‘rigid band’ approximation, quenching occurs when the filling with

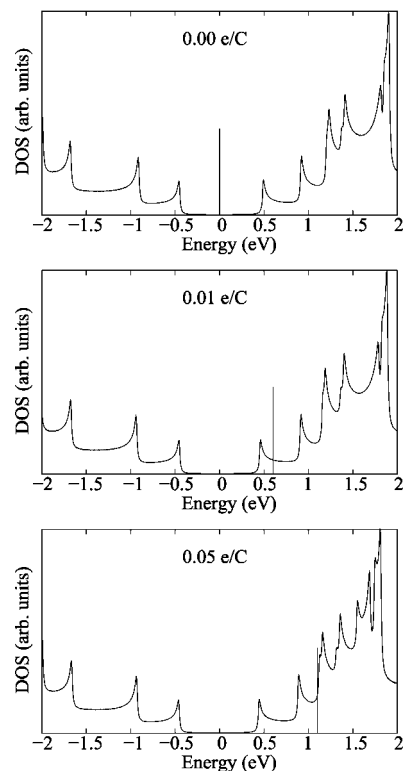


Figure 8. The calculated DOS of (6,5) for the neutral case and for two doping levels: 0.01 e/C and 0.05 e/C. The vertical lines show the position of the Fermi energy.

electrons (or holes) reaches the peak in the DOS corresponding to the VHS involved in the resonant transition.

In order to model the Raman profile by theoretical calculations, without knowing the necessary matrix elements, the following calculation was carried out. Within the rigid band approximation, the change of the electrode potential mimics the change of the Fermi level. By changing the Fermi level, the occupancy of the VHS is changed, and this can be calculated for electrons as well as for holes. Full bleaching occurs when all the states in the DOS for the given Van Hove singularity are occupied by electrons or holes. We approximated the Raman intensity simply by calculating the unoccupied part of the given band, which is, in our case, involved in the E_{22} transition. Our procedure was as follows: we extracted at first the band involved in the E_{22} transition from the DFT calculated electronic band structure and then integrated its occupied part up to the Fermi level, as a function of the Fermi level. The integration was normalized, setting the full integral to 1. Because the DOS has no electron–hole symmetry, the procedure was carried out separately in the positive and negative directions of the E_F shifts. Then, the remaining normalized integral for the nonoccupied part as a function of the Fermi level mimics the experimental Raman profile. Figure 9 shows the results for the (6,5) tube. The solid line is the theoretical profile, in which the Fermi level for the undoped case was set to -0.5 V vs Fc/Fc^+ (see Figure 5 and the discussion thereof). The dashed line and the markers are experimental data for the 2.18 eV excitation (as in Figure 5).

Although the details (shape of the plateau, sharpness of the drop) are different, the main characteristics are similar. Therefore, we can assume that, neglecting the exact shape of the intensity/potential profile, the width of the experimental ‘plateau’ after which the intensity starts to drop correlates with ΔE_{22} .

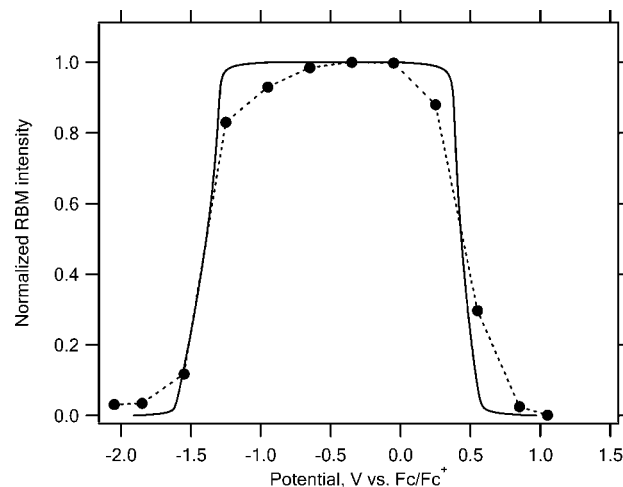


Figure 9. Intensity of the RBM-line as a function of the applied electrode potential for the (6,5) tube at the 2.18 eV laser excitation. The intensities were normalized by assigning 1 to the maximum RBM intensity. The solid line is the theoretically calculated Raman profile for the (6,5) tube, as discussed in the text. The markers and dashed line are experimental data.

Looking at Table 2 it is easy to understand why the profiles for (7,5) and (8,3) are somewhat sharper than those for (6,4) and (6,5).

5. Conclusion

A detailed spectroscopic, spectroelectrochemical, and theoretical study of selected single-walled carbon nanotubes in an enriched nanotube sample is given. The samples of CoMoCat tubes have been enriched with (6,5) tubes *via* density-gradient ultracentrifugation. As electrode material, thin solid films of quasi-isolated nanotubes were fabricated from the solution of sorted nanotubes by vacuum filtration and extraction with water. Vis–NIR and Raman spectroscopic studies were combined with a theoretical analysis of the electronic and vibrational structure of selected (n,m) tubes by using density functional theory. Besides the detailed analysis of the most abundant tubes (6,5), the experimental and theoretical data for tubes (5,3), (6,4), (7,3), (7,5), (8,3), and (9,1) were discussed as well.

The in situ Raman spectroelectrochemical investigation was focused on the effects of electrochemical p/n-doping on the electronic state of the enriched nanotubes. The experimental analysis of the intensities and frequencies of the radial breathing mode and the tangential displacement modes were correlated with the theoretically calculated optical transition energies and Raman frequencies. It was demonstrated that the electrochemical charging is a useful tool for investigation of different doping-dependent effects in the electronic structure of carbon nanotubes. As the doping-sensitivity is a specific signature of SWNTs, it allows the exclusion of possible overlapping features of impurities (iodixanol) and it helps to assign certain unexpected Raman features, such as the peak at 422 cm^{-1} . The latter was assigned to the tube (5,3) whose concentration in the samples was too small to be detectable by a standard optical spectroscopic analysis. The strikingly different doping-sensitivity of the (6,5) tube in the CoMoCat and HiPco samples is another unique result from these spectroelectrochemical investigations. Our data show that the effect of the tube diameter and the band gap on the absolute potential of the Fermi level is much smaller than it was reported earlier based on electrochemical¹⁴ and chemical³¹ doping studies of SWNTs. The measured Raman intensity vs

electrode potential profile of the (6,5) tube was modeled theoretically. The occupied part of the DOS was investigated within the rigid band approximation, as a function of the Fermi level. Good agreement was found for the measured and calculated profiles.

Acknowledgment. This work was supported by IFW Dresden, by the Czech Ministry of Education Youth and Sports (contract No. LC-510), by the Academy of Sciences of the Czech Republic (contracts IAA 400400804 and KAN 200100801) and by OTKA Grants No. K60576, F68852, and NI67702 in Hungary. V.Z. acknowledges the Bolyai Research Fellowship of the Hungarian Academy of Sciences. Additional support from an Alfred P. Sloan Research Fellowship (M.C.H.) and a Natural Sciences and Engineering Research Council of Canada Fellowship (A.A.G.) is gratefully acknowledged. This work was also funded by the U.S. Army Telemedicine and Advanced Technology Research Center under Award Number DAMD17-05-1-0381, the U.S. Department of Energy under Award Number DE-FG02-03ER15457, and the U.S. National Science Foundation under Award Numbers EEC-0647560 and DMR-0706067. The authors thank Alexander Manasson for assistance with sample preparation.

References and Notes

- (1) Sumanasekera, G. U.; Allen, J. L.; Fang, S. L.; Loper, A. L.; Rao, A. M.; Eklund, P. C. *J. Phys. Chem. B* **1999**, *103*, 4292.
- (2) Claye, A.; Nemes, N. M.; Janossy, A.; Fischer, J. E. *Phys. Rev. B* **2000**, *62*, R4845–R4848.
- (3) Kavan, L.; Rapt, P.; Dunsch, L. *Chem. Phys. Lett.* **2000**, *328*, 363.
- (4) Kavan, L.; Dunsch, L. *ChemPhysChem* **2007**, *8*, 974.
- (5) Das, A.; Sood, A. K.; Govindaraj, A.; Saitta, A. M.; Lazzeri, M.; Mauri, F.; Rao, C. N. R. *Phys. Rev. Lett.* **2007**, *99*, 136803.
- (6) Wang, Z.; Pedrosa, H.; Krauss, T.; Rothberg, L. *Phys. Rev. Lett.* **2006**, *96*, 047403.
- (7) Telg, H.; Maultzsch, J.; Reich, S.; Hennrich, F.; Thomsen, C. *Phys. Rev. Lett.* **2004**, *93*, 177401.
- (8) Fantini, C.; Jorio, A.; Souza, M.; Strano, M. S.; Dresselhaus, M. S.; Pimenta, M. A. *Phys. Rev. Lett.* **2004**, *93*, 147406.
- (9) Son, H.; Reina, A.; Samsonidze, G. G.; Saito, R.; Jorio, A.; Dresselhaus, M. S.; Kong, J. *Phys. Rev. B* **2006**, *74*, 073406.
- (10) Kavan, L.; Kalbac, M.; Zúkalova, M.; Dunsch, L. *Phys. Rev. Lett.* **2007**, *98*, 019701.
- (11) Fantini, C.; Jorio, A.; Santos, P. S.; Peressinotto, V. S. T.; Pimenta, M. A. *Chem. Phys. Lett.* **2007**, *439*, 138.
- (12) Jorio, A.; Santos, P. S.; Riberiro, M. C. C.; Fantini, C.; Souza, M.; Viera, J. P. M.; Furtado, C. A.; Jiang, J.; Saito, R.; Balzano, L.; Resasco, D. E.; Pimenta, M. A. *Phys. Rev. B* **2005**, *72*, 075207.
- (13) Pfeiffer, R.; Simon, F.; Kuzmany, H.; Popov, V. N. *Phys. Rev. B* **2005**, *72*, 161404(R)–1614044.
- (14) Okazaki, K.; Nakato, Y.; Murakoshi, K. *Phys. Rev. B* **2003**, *68*, 035434.
- (15) Cronin, S. B.; Barnett, R.; Tinkham, M.; Chou, S. G.; Rabin, O.; Dresselhaus, M. S.; Swan, A. K.; Unlu, M. S.; Goldberg, B. B. *Appl. Phys. Lett.* **2004**, *84*, 2052.
- (16) Kavan, L.; Kalbac, M.; Zúkalova, M.; Dunsch, L. *J. Phys. Chem. B* **2005**, *109*, 19613.
- (17) Kavan, L.; Kalbac, M.; Zúkalova, M.; Dunsch, L. *Phys. Stat. Sol. (b)* **2006**, *243*, 3130.
- (18) Arnold, M. S.; Green, A. A.; Hulvat, J. F.; Stupp, S. I.; Hersam, M. C. *Nature Nanotechnol.* **2006**, *1*, 60.
- (19) Green, A. A.; Hersam, M. C. *Mater. Today* **2007**, *10*, 59.
- (20) Kavan, L.; Dunsch, L. *Nano Lett.* **2003**, *3*, 969.
- (21) Kavan, L.; Rapt, P.; Dunsch, L.; Bronikowski, M. J.; Willis, P.; Smalley, R. E. *J. Phys. Chem. B* **2001**, *105*, 10764.
- (22) Kresse, G.; Hafner, J. *Phys. Rev. B* **1993**, *48*, 13115.
- (23) Kürti, J.; Zólyomi, V.; Kertesz, M.; Sun, G. *New J. Phys.* **2003**, *5*, 125.1125.21.
- (24) Kürti, J.; Zólyomi, V.; Kertesz, M.; Sun, G. Y.; Baughman, R. H.; Kuzmany, H. *Carbon* **2004**, *42*, 971.
- (25) Weisman, R. B.; Bachilo, S. M. *Nano Lett.* **2003**, *3*, 1235.
- (26) Barone, V.; Peralta, J. E.; Wert, M.; Heyd, J.; Scuseria, G. E. *Nano Lett.* **2005**, *5*, 1621.
- (27) Kavan, L.; Kalbac, M.; Zúkalova, M.; Krause, M.; Dunsch, L. *ChemPhysChem* **2004**, *5*, 274.
- (28) Kalbac, M.; Kavan, L.; Zúkalova, M.; Dunsch, L. *Adv. Funct. Mater.* **2005**, *15*, 418.
- (29) Takeda, N.; Murakoshi, K. *Anal. Bioanal. Chem.* **2007**, *388*, 108.
- (30) O'Connell, M. J.; Sivaram, S.; Doorn, S. K. *Phys. Rev. B* **2004**, *69*, 235415.
- (31) O'Connell, M. J.; Eibergen, E. E.; Doorn, S. K. *Nature Mat.* **2005**, *4*, 412.
- (32) Paolucci, D.; Franco, M. M.; Iurio, M.; Marcaccio, M.; Prato, M.; Zerbetto, F.; Penicaud, A.; Paolucci, F. *J. Am. Chem. Soc.* **2008**, *130*, 7395.
- (33) Barone, V.; Peralta, J. E.; Uddin, J.; Scuseria, G. E. *J. Chem. Phys.* **2008**, *124*, 024709.
- (34) Shan, B.; Cho, K. *Phys. Rev. Lett.* **2005**, *94*, 236602.
- (35) McDonald, T. J.; Svedruzic, D.; Kim, Y. H.; Blackburn, J. L.; Zhang, S. B.; King, P. W.; Heben, M. J. *Nano Lett.* **2007**, *7*, 3528.
- (36) Jorio, A.; Souza Filho, A. G.; Dresselhaus, G.; Dresselhaus, M. S.; Swan, A. K.; Unlu, M. S.; Goldberg, B. B.; Pimenta, M. A.; Hafner, J. H.; Lieber, C. M.; Saito, K. *Phys. Rev. B* **2002**, *65*, 155412.

JP800481B